Journal of Computational Physics 290 (2015) 157–168

Contents lists available at ScienceDirect

Journal of Computational Physics

www.elsevier.com/locate/jcp

Numerical solution of an inverse obstacle scattering problem with near-field data ☆

Peijun Li *, Yuliang Wang

Department of Mathematics, Purdue University, West Lafayette, IN 47907, USA

ARTICLE INFO

Article history:
Received 30 September 2014
Received in revised form 26 January 2015
Accepted 1 March 2015
Available online 5 March 2015

Keywords:
Inverse obstacle scattering
Near-field imaging
Transformed field expansion
Subwavelength resolution

ABSTRACT

Consider the scattering of an arbitrary time-harmonic incident wave by a sound soft obstacle. In this paper, a novel method is presented for solving the inverse obstacle scattering problem of the two-dimensional Helmholtz equation, which is to reconstruct the obstacle surface by using the near-field data. The obstacle is assumed to be a small and smooth perturbation of a disc. The method uses the transformed field expansion to reduce the boundary value problem into a successive sequence of one-dimensional problems which are solved in closed forms. By dropping the higher order terms in the power series expansion and truncating the infinite linear system for the first order term, the inverse problem is linearized and an approximate but explicit formula is obtained between the Fourier coefficients of the solution and data. A nonlinear correction algorithm is introduced to improve the accuracy of the reconstructions for large deformations. Numerical examples show that the method is simple, efficient, and stable to reconstruct the obstacle with subwavelength resolution.

1. Introduction

Obstacle scattering problems are concerned with the effect that a bounded scatterer has on an incident field. These problems are fundamental in a wide range of applications [9,12,13] such as radar and sonar, geophysical exploration, medical imaging, nondestructive testing, and near-field optics. Given the incident wave, the direct obstacle scattering problem is to determine the scattered wave for the known obstacle. This paper is concerned with the inverse obstacle scattering problem, which is to reconstruct its surface from the field measured on a circle surrounding the obstacle.

The inverse problem is challenging due to its high nonlinearity and severe ill-posedness. A number of numerical methods have been proposed to overcome the issues. They can be broadly classified into two categories: nonlinear optimization based iterative methods [15,18,20,21] and imaging based direct methods [8,11,17,19,24,25]. The iterative methods require good initial guesses and are computationally expensive as a sequence of direct and adjoint problems need to be solved at each step of iterations. The direct methods require no a priori information on the obstacles and are computationally efficient, but the reconstructions may not be as accurate as those iterative methods.

It is known that conventional reconstruction methods cannot achieve super-resolution because of using only far-field data, i.e., data measured at a distance which is a few wavelengths or longer away from the obstacle. According to the Rayleigh criterion, the resolution of far-field imaging is limited roughly by one half the wavelength of the incident field

☆ The research was supported in part by the NSF grant DMS-1151308.
* Corresponding author.
E-mail addresses: lipeijun@math.purdue.edu (P. Li), wang2049@math.purdue.edu (Y. Wang).

http://dx.doi.org/10.1016/j.jcp.2015.03.004
0021-9991/

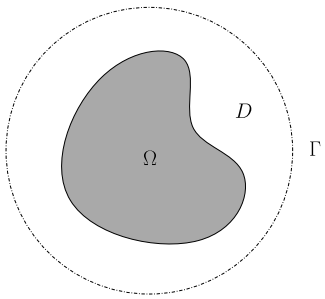

Fig. 1. Geometry of the problem. The obstacle is represented by the domain Ω and the measurement is taken at the circle Γ.

[13], which is known as the diffraction limit. By collecting data in the near-field zone, one may break the diffraction limit and obtain images with subwavelength resolution. This is referred to as near-field imaging [13] and has led to emerging applications in modern science and technology such as nanotechnology, biology, information storage, and surface chemistry.

Recently a novel approach has been developed for solving a variety of inverse scattering problems in near-field imaging, which include infinite rough surfaces [2,3], diffraction gratings [1,10], obstacles [22], and interior cavities [23]. The method begins with the transformed field expansion, which reduces the high dimensional boundary value problems to a successive sequence of one-dimensional two-point boundary value problems in the frequency domain, where analytical solutions are obtained in closed forms. By dropping higher order terms in the power series expansion, the inverse problems are linearized and explicit reconstruction formulas are obtained. The method requires only one incident field at a fixed angle and frequency. Numerical experiments have shown that the method is simple, efficient, and stable to reconstruct the surfaces with subwavelength resolution. We refer to [16] for a related three-dimensional inverse obstacle scattering problem by using the factorization method and to [5–7] for the inverse problems in near-field imaging of local displacement on an infinite ground plane.

In [22], the incident field is assumed to be an incoming cylindrical wave. Mathematically, it is a good choice in view of the problem geometry as it facilitates the analysis and leads to an explicit reconstruction formula. However, this special incident wave may not be easily realized in practice. In this work, we extend the method to arbitrary time harmonic incident waves which include the commonly used plane wave and the point source wave. This nontrivial extension makes the method more universal in a wide range of practical situations. Although we focus on the two-dimensional Helmholtz equation in this work, the method can be also extended to deal with the three-dimensional Helmholtz and Maxwell's equations.

The outline of the paper is as follows. In Section 2, the inverse obstacle scattering problem is introduced and a simple uniqueness result is given. Section 3 is devoted to the transformed field expansion for the boundary value problem whose solution is obtained in a closed form. The reconstruction formula is derived and a nonlinear correction algorithm is described in Section 4. Numerical results are presented in Section 5. The paper is concluded with general remarks and directions for future research in Section 6.

2. The inverse scattering problem

As seen in Fig. 1, let the obstacle be a small and smooth perturbation of a disk in $\mathbb{R}^2$. In the polar coordinate, it can be described by a domain

$$\Omega = \{(r,\theta) : 0 < r < a + f(\theta), \theta \in [0, 2\pi)\},$$

where $a > 0$ is a constant representing the radius of the unperturbed disk and $f(\theta)$ is the obstacle surface function. We assume that $f \in C^2(\mathbb{R})$ is a 2π-periodic function whose infinity norm is small comparing to the wavelength λ of the incident field. Hence it can be written as

$$f(\theta) = \varepsilon g(\theta),$$

where $\varepsilon > 0$ is a small perturbation parameter and g is the obstacle profile function such that $\|g\|_\infty = \mathcal{O}(\lambda)$.

In the exterior domain $\mathbb{R}^2 \setminus \bar{\Omega}$, the space is assumed to be filled with a homogeneous medium characterized by a constant wavenumber $\kappa = 2\pi/\lambda$. An incoming wave $u^{\text{inc}}(r,\theta)$ is incident on the obstacle and generates the scattered wave u^{sca}. Clearly the total field u consists of the incident field and the scattered field, i.e., $u = u^{\text{inc}} + u^{\text{sca}}$. For a sound soft obstacle, the total field vanishes on the obstacle surface, i.e.,

$$u = 0 \quad \text{on } \partial\Omega. \tag{2.1}$$

Given the incident field u^{inc} and the obstacle surface function f, the direct problem is to determine the total field u. This paper is focused on the inverse problem: given the incident field u^{inc}, reconstruct the surface function f from the total field u measured at a circle

$$\Gamma = \{(b,\theta) : r = b > a + \|f\|_\infty, \theta \in [0, 2\pi)\}.$$

We shall derive a transparent boundary condition for u on Γ. Denote by D the domain which is enclosed by the two boundaries of $\partial\Omega$ and Γ. The scattered field u^{sca} satisfies the two-dimensional Helmholtz equation

$$\left(\Delta + \kappa^2\right) u^{\text{sca}} = 0 \quad \text{in } D. \tag{2.2}$$

It follows from the separation of variables in the exterior of Γ and the bounded outgoing wave condition for the scattered field that we have the expansion

$$u^{\text{sca}}(r,\theta) = \sum_{n\in\mathbb{Z}} A_n H_n^{(1)}(\kappa r)\exp(\mathrm{i}n\theta), \quad r \geq b, \tag{2.3}$$

where $H_n^{(1)}$ is the n-th order Hankel function of the first kind. Taking ∂_r on both sides of (2.3) and evaluating at Γ yield the transparent boundary condition

$$(\partial_r - \mathscr{B})\, u^{\text{sca}}(b,\theta) = 0, \tag{2.4}$$

where $\mathscr{B}$ is a linear operator satisfying

$$\mathscr{B}[\exp(\mathrm{i}n\theta)] = \frac{H_n^{(1)'}(\kappa b)}{H_n^{(1)}(\kappa b)}\exp(\mathrm{i}n\theta).$$

The incident field u^{inc} is required to satisfy the Helmholtz equation

$$\left(\Delta + \kappa^2\right) u^{\text{inc}} = 0 \quad \text{in } D. \tag{2.5}$$

It can be verified that a wide range of waves, including the plane wave, the incoming cylindrical wave, and the wave generated by a point source in the exterior of Γ, satisfy (2.5). As a 2π-periodic function of θ, the incident wave u^{inc} is assumed to admit the following Fourier series expansion on Γ:

$$u^{\text{inc}}(b,\theta) = \sum_{n\in\mathbb{Z}} A_n \exp(\mathrm{i}n\theta), \quad \partial_r u^{\text{inc}}(b,\theta) = \sum_{n\in\mathbb{Z}} A_n' \exp(\mathrm{i}n\theta), \tag{2.6}$$

where A_n and A_n' are constants.

Adding (2.2) and (2.5), we have

$$\left(\Delta + \kappa^2\right) u = 0 \quad \text{in } D. \tag{2.7}$$

Taking $\partial_r - \mathscr{B}$ on (2.6) and adding to (2.4) yield a transparent boundary condition for the total field:

$$(\partial_r - \mathscr{B})\, u(b,\theta) = \rho(\theta), \tag{2.8}$$

where

$$\rho(\theta) = \sum_{n\in\mathbb{Z}} \left[A_n' - \frac{H_n^{(1)'}(\kappa b)}{H_n^{(1)}(\kappa b)} A_n \right] \exp(\mathrm{i}n\theta). \tag{2.9}$$

Following a similar proof in [23], we may show a uniqueness result for the inverse problem.

Theorem 2.1. *Let Ω_1, Ω_2 be two obstacles defined by the same base radius a and two surface functions f_1, f_2 such that*

$$\kappa < j_{0,1}\sqrt{\frac{\pi}{A}},$$

where $j_{0,1} \approx 2.4048$ is the first zero of the Bessel function of the first kind with order zero J_0 and A is the area enclosed between Ω_1, Ω_2, given explicitly by

$$A = \frac{1}{2}\int_0^{2\pi} \left|(a + f_1(\theta))^2 - (a + f_2(\theta))^2\right| \mathrm{d}\theta.$$

Let $u_1(b,\cdot), u_2(b,\cdot)$ be the total fields at Γ corresponding to Ω_1, Ω_2, respectively. If $u_1(b,\cdot) = u_2(b,\cdot)$, then $f_1 = f_2$.

3. Transformed field expansion

In this section, we apply the transformed field expansion to reduce the two-dimensional boundary value problem (2.7), (2.1) and (2.8) into a successive sequence of one-dimensional two-point boundary value problems.

We begin with the change of variables

$$\tilde{r} = \frac{hr - bf(\theta)}{h - f(\theta)}, \quad \tilde{\theta} = \theta,$$

which transforms the domain D to the annulus

$$\tilde{D} = \{(\tilde{r}, \tilde{\theta}) : a < \tilde{r} < b, \tilde{\theta} \in [0, 2\pi)\}.$$

Here

$$h = b - a$$

is denoted as the measurement distance. To simplify calculations and notations, we apply another set of change of variables

$$\hat{\tilde{r}} = \kappa\tilde{r}, \quad \hat{\tilde{\theta}} = \tilde{\theta}, \quad \hat{\tilde{u}}\left(\hat{\tilde{r}}, \hat{\tilde{\theta}}\right) = \tilde{u}\left(\tilde{r}, \tilde{\theta}\right),$$

$$\hat{a} = \kappa a, \quad \hat{b} = \kappa b, \quad \hat{f} = \kappa f, \quad \hat{g} = \kappa g, \quad \hat{h} = \kappa h,$$

which normalizes the scale of the problem with respect to the wavenumber. Using the chain rule for partial derivatives in (2.7) and dropping the tildes and hats on all variables afterwards, we obtain

$$\left(c_1\partial_{rr} + c_2\frac{\partial_r}{r} + c_3\frac{\partial_{r\theta}}{r} + c_4\frac{\partial_{\theta\theta}}{r^2} + c_5\right)u(r,\theta) = 0 \quad \text{in } D, \tag{3.1}$$

where

$$\begin{aligned}
c_1 &= h^2 + 2hpf + p^2\left[f^2 + (f')^2\right],\\
c_2 &= h^2 + h\left[(p-1)f - pf''\right] - p\left[f^2 - 2(f')^2 + ff''\right],\\
c_3 &= 2p\left(-hf' + ff'\right),\\
c_4 &= h^2 - 2hf + f^2,\\
c_5 &= h^2 + 2h(p-1)f + \left(p^2 - 4p + 1\right)f^2 + \frac{2\left(p - p^2\right)f^3}{h} + \frac{p^2f^4}{h^2},
\end{aligned}$$

and the variable

$$p = \frac{b}{r} - 1$$

is introduced to simplify the expressions.

Next we reduce the boundary value problem (3.1), (2.1) and (2.8) into a successive sequence of simpler boundary value problems. Due to the small perturbation assumption $f = \varepsilon g$, we may consider a power series expansion for the solution in terms of ε:

$$u(r,\theta) = \sum_{k=0}^{\infty} u_k(r,\theta)\varepsilon^k. \tag{3.2}$$

Substituting (3.2) into (3.1) and replacing f with εg in the coefficients c_j, we may obtain the recurrence equation

$$(\Delta + 1)\, u_k = -v_k, \tag{3.3}$$

where

$$v_k = \sum_{j=1}^{4} d_j u_{k-j} \tag{3.4}$$

and

$$\begin{aligned}
d_1 &= \frac{1}{h}\left\{2pg\partial_{rr} + \left[(p-1)g - pg''\right]\frac{\partial_r}{r} - 2pg'\frac{\partial_{r\theta}}{r} - 2g\frac{\partial_{\theta\theta}}{r^2} + 2(p-1)g\right\},\\
d_2 &= \frac{1}{h^2}\left\{p^2\left[g^2 + (g')^2\right]\partial_{rr} + p\left[gg'' - 2(g')^2 - g^2\right]\frac{\partial_r}{r} + 2pgg'\frac{\partial_{r\theta}}{r} + g^2\frac{\partial_{\theta\theta}}{r^2} + \left(p^2 - 4p + 1\right)g^2\right\},
\end{aligned}$$

$$d_3 = \frac{1}{h^3}\left[2(p - p^2)g^3\right],$$
$$d_4 = \frac{1}{h^4}(p^2 g^4).$$

Similarly, we have from the boundary conditions (2.1) and (2.8) that

$$u_k(a,\theta) = 0, \quad k \geq 0 \tag{3.5}$$

and

$$(\partial_r - \mathscr{B})\, u_k(b,\theta) = \rho_k(\theta), \tag{3.6}$$

where

$$\rho_0 = \rho, \quad \rho_1 = -\left(\frac{g}{h}\right)[\mathscr{B}u_0(b,\theta) + \rho], \quad \rho_k = -\left(\frac{g}{h}\right)\mathscr{B}u_{k-1}(b,\theta),\ k \geq 2. \tag{3.7}$$

It is understood that $u_k = 0$ for $k < 0$ in all the recurrence relations.

It is easy to note that u_k, v_k, and ρ_k are all 2π-periodic functions in θ. Taking the Fourier transform with respect to θ of the boundary value problem (3.3), (3.5) and (3.6) leads to the following two-point boundary value problem:

$$L_n u_k^{(n)}(r) = -v_k^{(n)}(r), \quad r \in (a,b), \tag{3.8a}$$
$$u_k^{(n)}(a) = 0, \tag{3.8b}$$
$$\left(\frac{\mathrm{d}}{\mathrm{d}r} - \frac{H_n^{(1)\prime}(b)}{H_n^{(1)}(b)}\right) u_k^{(n)}(b) = \rho_k^{(n)}, \tag{3.8c}$$

where the superscript (n) is the n-th Fourier coefficients and L_n is the Bessel operator of order n.

Using the variation of parameters, we may solve (3.8) and write the solution as

$$u_k^{(n)}(r) = c_1 H_n^{(1)}(r) + c_2 H_n^{(2)}(r) + \int_a^r \left[H_n^{(1)}(r)H_n^{(2)}(s) - H_n^{(1)}(s)H_n^{(2)}(r)\right] \frac{v_k^{(n)}(s)}{W(s)}\mathrm{d}s, \tag{3.9}$$

where c_1, c_2 are constants and

$$W(s) = H_n^{(1)}(s)H_n^{(2)\prime}(s) - H_n^{(1)\prime}(s)H_n^{(2)}(s) = -\frac{4\mathrm{i}}{\pi s} \tag{3.10}$$

is the Wronskian of $H_n^{(1)}$ and $H_n^{(2)}$ [14]. Substituting (3.9) into (3.8b) and (3.8c) yields

$$c_2 = \frac{H_n^{(1)}(b)\rho_k^{(n)}}{W(b)} + \int_a^b \frac{H_n^{(1)}(s)v_k^{(n)}(s)}{W(s)}\,\mathrm{d}s, \quad c_1 = -\frac{H_n^{(2)}(a)}{H_n^{(1)}(a)}c_2.$$

Substituting c_1, c_2 into (3.9), we obtain the solution

$$u_k^{(n)}(r) = \Phi_n(r,b)\rho_k^{(n)} + \int_a^b \Phi_n(r,s)v_k^{(n)}(s)\,\mathrm{d}s, \quad r \in [a,b], \tag{3.11}$$

where

$$\Phi_n(r,s) = \frac{1}{W(s)}\begin{cases} H_n^{(1)}(r)E_n(s), & s \leq r, \\ H_n^{(1)}(s)E_n(r), & s \geq r, \end{cases}$$
$$E_n(z) = H_n^{(2)}(z) - \frac{H_n^{(2)}(a)}{H_n^{(1)}(a)}H_n^{(1)}(z).$$

Using (3.11) and the recurrence relations (3.4), (3.6), we may solve u_k for each k. For the purpose of linearizing the problem, we shall derive more explicit forms for $k = 0, 1$. For $k = 0$, we obtain from (3.4) that

$$v_0^{(n)} = 0,$$

and from (3.7), (2.9) that

$$\rho_0^{(n)} = A_n' - \frac{H_n^{(1)\prime}(b)}{H_n^{(1)}(b)}A_n. \tag{3.12}$$

Using (3.11) yields

$$u_0^{(n)}(r) = \Phi_n(r,b)\rho_0^{(n)}. \tag{3.13}$$

Now u_0 is obtained, we use the recurrence relation (3.4) and the convolution theorem to obtain

$$v_1^{(n)}(r) = \sum_{m\in\mathbb{Z}} V_{n,m}(r) g^{(n-m)}, \tag{3.14}$$

where

$$V_{n,m}(r) = \frac{1}{h}\left\{2p\partial_{rr} + \left[(n^2-m^2+1)p-1\right]\frac{\partial_r}{r} + \left[\frac{2m^2}{r^2} + 2(p-1)\right]\right\}\Phi_m(r,b)\rho_0^{(m)}. \tag{3.15}$$

Similarly we obtain from (3.7) that

$$\rho_1^{(n)} = \sum_{m\in\mathbb{Z}} \Psi_m g^{(n-m)}, \tag{3.16}$$

where

$$\Psi_m = -\frac{1}{h}\left[\frac{H_m^{(1)\prime}(b)}{H_m^{(1)}(b)}\Phi_m(b,b) + 1\right]\rho_0^{(m)}. \tag{3.17}$$

Substituting (3.14) and (3.16) into (3.11) at $r = b$, we obtain an infinitely dimensional linear system equations:

$$u_1^{(n)}(b) = \sum_{m\in\mathbb{Z}} S_{n,m} g^{(n-m)}, \tag{3.18}$$

where

$$S_{n,m} = \Phi_n(b,b)\Psi_m + \int_a^b \Phi_n(b,s)V_{n,m}(s)\,\mathrm{d}s. \tag{3.19}$$

To solve the infinite linear system (3.18), we truncate it up to the N-th Fourier coefficients and obtain the following approximate finitely dimensional linear system of equations:

$$M\mathbf{g} = \mathbf{u}, \tag{3.20}$$

where $M \in \mathbb{C}^{(2N+1)\times(2N+1)}$, and $\mathbf{g}, \mathbf{u} \in \mathbb{C}^{2N+1}$ are given by

$$M(m,n) = S_{m,m-n}, \quad \mathbf{g}(m) = g^{(m)}, \quad \mathbf{u}(n) = u_1^{(n)}(b), \tag{3.21}$$

for $-N \le m,\ n \le N$. Notice that the entries of M depend only on the incident field and are independent of g. The right-hand-side $\mathbf{u}$ can be approximated by $u - u_0$, where u_0 is also independent of g. Hence the inverse problem is linearized and can be approximately solved by inverting the linear system (3.20).

In the following, we derive more explicit forms for u_0 and M for commonly used incident fields.

Example 3.1. The incident field in [22] is an incoming cylindrical wave, i.e.,

$$u^{\mathrm{inc}}(r,\theta) = H_0^{(2)}(r).$$

From (2.6), we have

$$A_n = H_n^{(2)}(b)\delta_{0n}, \quad A_n' = H_n^{(2)\prime}(b)\delta_{0n},$$

where δ is the Kronecker delta notation. Substituting into (3.12) and using the Wronskian formula yields

$$\rho_0^{(n)} = -\frac{4\mathrm{i}}{\pi b H_n^{(1)}(b)}\delta_{0n}. \tag{3.22}$$

Substituting (3.22) into (3.13) yields a simple form for u_0:

$$u_0(r,\theta) = E_0(r).$$

In view of (3.15), (3.17), (3.19), (3.21), and (3.22), it is clear to note that M becomes a diagonal matrix and (3.20) reduces to the same formula as that in [22].

Example 3.2. Let the incident field be a plane wave propagating in the positive x direction. In the polar coordinates, we have

$$u^{\text{inc}}(r,\theta) = e^{\mathrm{i}r\cos\theta},$$

which has the following expansion

$$u^{\text{inc}}(r,\theta) = \sum_{n\in\mathbb{Z}} \mathrm{i}^n J_n(r) e^{\mathrm{i}n\theta}.$$

Here J_n is the n-th order Bessel function of the first kind. By (2.6) we have

$$A_n = \mathrm{i}^n J_n(b), \quad A_n' = \mathrm{i}^n J_n'(b).$$

Substituting A_n, A_n' into (3.12) and using the Wronskian formula (3.10) yield

$$\rho_0^{(n)} = \frac{2\mathrm{i}^{n-1}}{\pi b H_n^{(1)}(b)}. \tag{3.23}$$

Substituting (3.23) into (3.13) leads to

$$u_0^{(n)} = \frac{\mathrm{i}^n}{2} E_n(r).$$

A more explicit form of M may be obtained by substituting (3.23) into (3.15), (3.17), (3.19), and (3.21).

Example 3.3. Let the incident field be generated by a point source located at (r_0,θ_0), which gives

$$u^{\text{inc}}(r,\theta) = H_0^{(1)}\left(\sqrt{r^2 - 2rr_0\cos(\theta-\theta_0) + r_0^2}\right)$$

and

$$\partial_r u^{\text{inc}}(r,\theta) = \frac{r - r_0\cos(\theta-\theta_0)}{\sqrt{r^2 - 2rr_0\cos(\theta-\theta_0) + r_0^2}} H_0^{(1)'}\left(\sqrt{r^2 - 2rr_0\cos(\theta-\theta_0) + r_0^2}\right).$$

It follows from (2.6) that we have

$$A_n = \frac{1}{2\pi}\int_0^{2\pi} u^{\text{inc}}(b,\theta) e^{-\mathrm{i}n\theta}\,\mathrm{d}\theta, \quad A_n' = \frac{1}{2\pi}\int_0^{2\pi} \partial_r u^{\text{i}}(b,\theta) e^{-\mathrm{i}n\theta}\,\mathrm{d}\theta,$$

which are not as explicit as the previous examples but can be computed by using numerical integrations.

In general, we may consider a linear combination of incident waves, e.g., plane waves propagating in different directions or multiple point sources. The corresponding matrix M and vector $\mathbf{u}$ in (3.20) are simply the linear combination of the matrices and vectors for each incident wave.

4. Reconstruction method

Based on (3.20), we are ready to present the reconstruction method which consists of linearization and nonlinear correction. Let the measurement data be represented by

$$u_\delta(b,\theta) = u(b,\theta) + \mathcal{O}(\delta), \tag{4.1}$$

where $u(b,\theta)$ is the exact value of the total field at Γ and δ is the noise level. Truncating the power series (3.2) at $k=1$, we have

$$u(b,\theta) = u_0(b,\theta) + \varepsilon u_1(b,\theta) + \mathcal{O}(\varepsilon^2).$$

Replacing $u(b,\theta)$ by its power series expansion in (4.1), we get

$$\varepsilon u_1(b,\theta) = u_\delta(b,\theta) - u_0(b,\theta) + \mathcal{O}(\varepsilon^2) + \mathcal{O}(\delta).$$

Dropping the terms $\mathcal{O}(\varepsilon^2)$ and $\mathcal{O}(\delta)$, and taking Fourier transform of the above equation yields an identity for the linearized inverse problem

$$\varepsilon u_1^{(n)}(b) = u_\delta^{(n)}(b) - u_0^{(n)}(b). \tag{4.2}$$

Substituting (4.2) into (3.20) and noticing $f = \varepsilon g$, we get

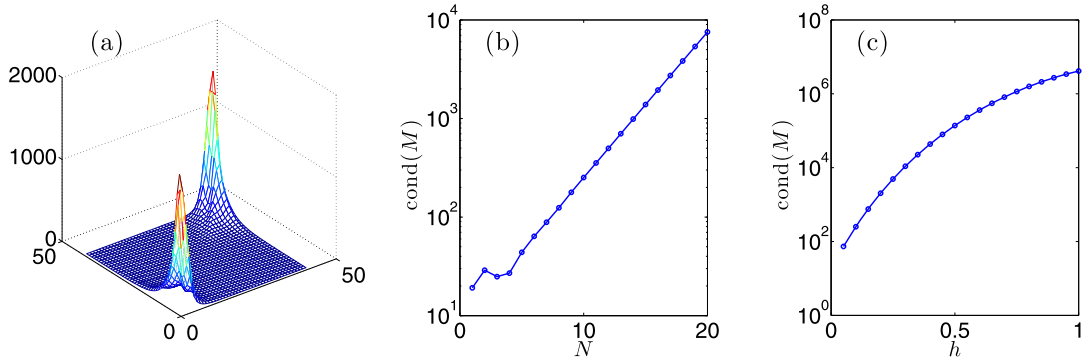

Fig. 2. A model problem with $a = \lambda/4$. (a) Plot of $|M_{ij}^{-1}|$ with $h = 0.1\lambda$ and $N = 20$; (b) plot of cond(M) for $h = 0.1\lambda$ and $N = 1, \cdots, 20$; (c) plot of cond(M) for $N = 10$ and $h \in [0.05, 1]\lambda$.

$$M\mathbf{f} = \mathbf{w}, \tag{4.3}$$

where

$$\mathbf{f}(m) = f^{(m)}, \quad \mathbf{w}(n) = u_\delta^{(n)} - u_0^{(n)}, \quad -N \le m, n \le N.$$

Solving the linear system of Eqs. (4.3), we obtain a reconstructed obstacle surface function $\mathbf{f}$:

$$f(\theta) = \mathrm{Re} \sum_{m=-K}^{K} \mathbf{f}(m) e^{\mathrm{i}m\theta}, \tag{4.4}$$

where $0 \le K \le N$ is the cut-off frequency and may be determined from some a priori information on the obstacle surface f or the noise level δ.

It is clear to note that the error in the reconstruction formula (4.4) consists of four parts:

(1) approximation error of an infinite linear system by a finite one in (3.20);
(2) linearization error $\mathcal{O}(\varepsilon^2)$ by dropping higher order terms in the power series expansion;
(3) noise in the measurement data $\mathcal{O}(\delta)$;
(4) approximation error of an infinite Fourier series by a finite one in (4.4).

The error estimate of our method requires a dedicated regularity analysis of the solution for the direct scattering problem and is beyond the scope of this paper. We will study the convergence analysis of the power series expansion and the error estimate of the reconstruction formula in a future work. A related work can be found in [4] for the convergence analysis of the power series and error estimates for solving a diffraction grating problem in near-field imaging.

Nevertheless we illustrate the ill-posedness of the inverse problem through numerical computation of the matrix M. Consider a model problem with $a = \lambda/4$. Fig. 2(a) shows the plot of $|M_{ij}^{-1}|$ with $h = 0.1\lambda$ and $N = 20$. Note the exponential growth towards the two corners of the matrix. This implies the error in the high Fourier mode of the data will be greatly amplified in the high Fourier mode of the reconstruction. Fig. 2(b) shows the plot of cond(M) as $h = 0.1\lambda$ is fixed and N runs from 1 to 20. Again we observe exponential growth, which implies the severe ill-posedness of the problem. Fig. 2(c) shows the plot of cond(M) as $N = 10$ is fixed and h varies from 0.05λ to 1λ. The growth of cond(M) as h increases implies the reconstruction is more stable and better resolution is achieved if h is smaller. This is consistent with the physical principle of near-field imaging.

Our reconstruction is a solution of an approximate linearized problem. Hence we may use it as a good initial guess and apply optimization algorithms to improve the accuracy. In fact, the explicitness of our method provides an intuitive iterative algorithm. Let f_0 be an initial guess constructed using (4.3) and (4.4). If u_{f_0} is the solution for the direct scattering problem with f_0 as the surface function, then we have

$$M\mathbf{f}_0 \approx \mathbf{u}_{f_0} - \mathbf{u}_0, \tag{4.5}$$

where

$$\mathbf{u}_{f_0}(n) = u_{f_0}^{(n)} \quad \text{and} \quad \mathbf{u}_0(n) = u_0^{(n)}.$$

Subtracting (4.5) from (4.3) yields

$$M(\mathbf{f} - \mathbf{f}_0) = \mathbf{u}_\delta - \mathbf{u}_{f_0},$$

where $\mathbf{u}_\delta(n) = u_\delta^{(n)}$. Hence we may obtain the updated Fourier coefficients

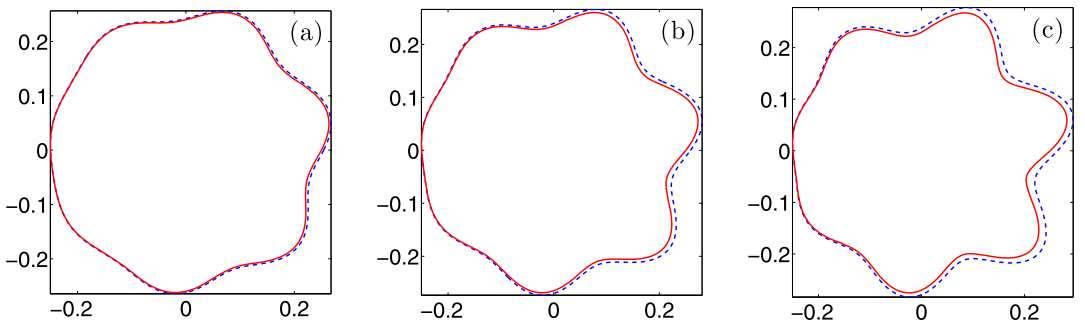

Fig. 3. Effect of ε: Exact (solid line) and reconstructed (dashed line) surface for $h = 0.15\lambda$, $\delta = 0$. (a) $\varepsilon = 0.02$; (b) $\varepsilon = 0.03$; (c) $\varepsilon = 0.04$.

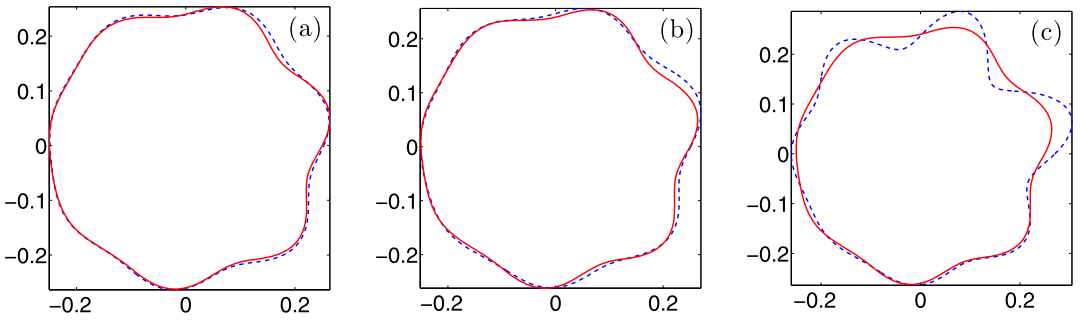

Fig. 4. Effect of δ: Exact (solid line) and reconstructed (dashed line) surface function for $\varepsilon = 0.02$, $h = 0.1\lambda$. (a) $\delta = 1\%$; (b) $\delta = 2\%$; (c) $\delta = 5\%$.

$$\mathbf{f}_1 = \mathbf{f}_0 + M^{-1}(\mathbf{u}_\delta - \mathbf{u}_{f_0}).$$

Repeating the above procedure yields an iterative algorithm

$$\mathbf{f}_{j+1} = \mathbf{f}_j + M^{-1}\big(\mathbf{u}_\delta - \mathbf{u}_{f_j}\big), \quad j = 0, 1, \ldots. \tag{4.6}$$

We mention that the nonlinear correction scheme (4.6) can be efficiently implemented since the matrix M remains unchanged for iterations.

5. Numerical examples

In this section we present numerical examples to show the effectiveness of our method and the dependence of the results on various parameters. The measurement data is taken at 127 uniformly distributed points on Γ, whose values are obtained by solving the corresponding direct scattering problem using the standard boundary integral equation method with 512 grid points on $\partial\Omega$. The direct scattering problem in the nonlinear correction scheme is also solved in the same manner. White noise is added to the data as

$$u_\delta(b, \theta_i) = u(b, \theta_i)(1 + \delta\mathcal{N}_i),$$

where $\mathcal{N}_i$ are values sampled from the standard normal distribution. Physical units are rescaled in terms of the wavelength in all figures.

5.1. Example 1

Consider an obstacle with surface given by $r(\theta) = a + f(\theta)$, where $a = \lambda/4$, $f = \varepsilon g$ and

$$g(\theta) = \lambda(0.5\sin 6\theta + 0.5\sin 7\theta).$$

The truncation level in (3.20) and (4.4) is taken as $N = K = 7$. The incident field is a single plane wave propagating in the direction $\theta = 0$.

Let the measurement height $h = 0.15\lambda$ and noise level $\delta = 0$ be fixed and consider the effects of the perturbation parameter ε. Fig. 3 shows the exact (solid) and the reconstructed (dashed) surface function for $\varepsilon = 0.02, 0.03$ and 0.04 respectively. The fine features of the obstacle are well reconstructed and subwavelength resolution is obtained in all three cases. However the accuracy of the reconstruction decreases as ε increases due to the linearization error in our model.

Next we fix $\varepsilon = 0.02$, $h = 0.1\lambda$ and consider the effects of the noise level δ. Fig. 4 shows the exact (solid) and the reconstructed (dashed) surface function for $\delta = 1\%, 2\%$ and 5% respectively. As expected the reconstruction deteriorates as δ increases.

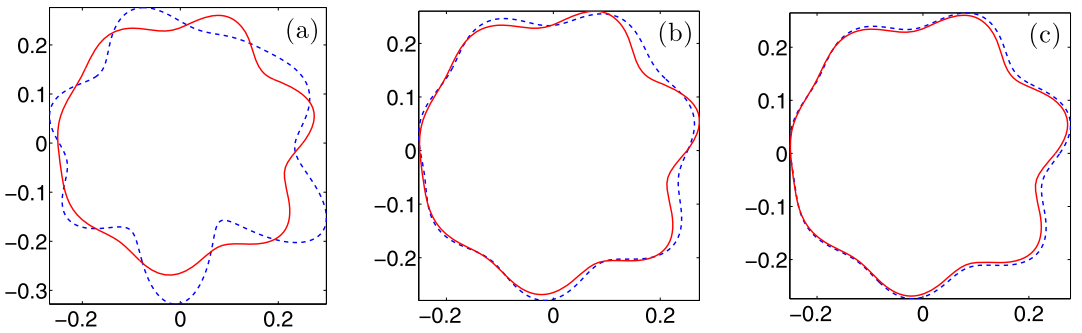

Fig. 5. Effect of h: Exact (solid line) and reconstructed (dashed line) surface function for $\varepsilon = 0.03$, $\delta = 3\%$ and (a) $h = 0.2\lambda$; (b) $h = 0.1\lambda$; (c) $h = 0.05\lambda$.

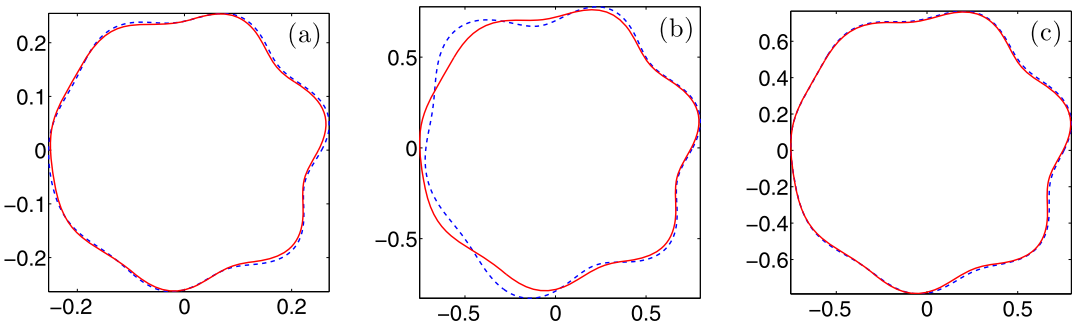

Fig. 6. Effect of incident field: Exact (solid line) and reconstructed (dashed line) surface function for $\varepsilon = 0.02$, $\delta = 1\%$, $h = 0.1$. (a) $\lambda = 1$, plane incident field from right; (b) $\lambda = 1/3$, plane incident field from right; (c) $\lambda = 1/3$, two plane incident field from both left and right.

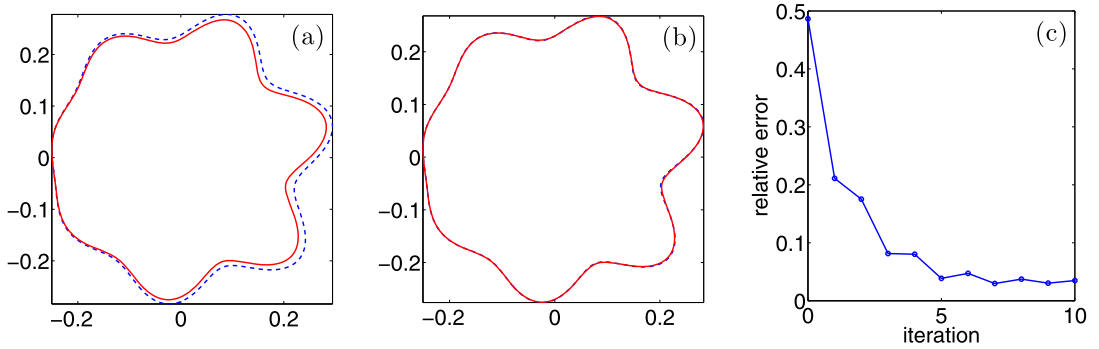

Fig. 7. Nonlinear correction algorithm: Exact (solid line) and reconstructed (dashed line) surface function for $\varepsilon = 0.04$, $\delta = 0$, $h = 0.1\lambda$. (a) Initial reconstruction; (b) after 2 iterations of nonlinear correction; (c) after 6 iterations of nonlinear correction.

Now we investigate the effect of the measurement distance h. Let $\varepsilon = 0.03$, $\delta = 3\%$ be fixed. Fig. 5 shows the exact (solid) and the reconstructed (dashed) surface function for $h = 0.2\lambda, 0.1\lambda$ and 0.05λ respectively. Clearly the accuracy of the reconstruction increases as h decreases, which confirms the principle of near-field imaging.

If the wavelength of the incident field is small with respect to the size of the obstacle, there will be a shadow behind the obstacle and the interaction between the wave and obstacle is weaker in this region. This could result in a poor reconstruction for this part of the boundary. Fig. 6(a) shows the exact (solid) and the reconstructed (dashed) profile for $\lambda = 1$, $\varepsilon = 0.02$, $\delta = 1\%$, $h = 0.1$ with a plane incident wave propagating at $\theta = \pi$. Fig. 6(b) shows the result for the same problem except the wavelength is decreased to $\lambda = 1/3$ (or equivalently, the size obstacle is increased three times). It can be seen of the deterioration of the reconstruction on the left part of the boundary. However, this deterioration can be fixed by adding another incident field sent from an opposite direction, i.e., from the left, as shown in Fig. 6(c).

We next test the proposed nonlinear correction algorithm. Fig. 7(a) shows the exact (solid) and the reconstructed (dashed) surface function for $\varepsilon = 0.04$, $\delta = 0$, $h = 0.1\lambda$ and without nonlinear correction. Fig. 7(b) shows the results after 10 iterations of nonlinear correction and Fig. 7(c) plots the relative L^2 error against the number of iterations. We observe the algorithm is effective at improving the accuracy if ε, δ are sufficiently small.

In the above experiments we assume the data can be measured in the whole circle surrounding the obstacle, i.e., we have full aperture data. However, the inverse scattering problems with limited aperture data are also important since the field

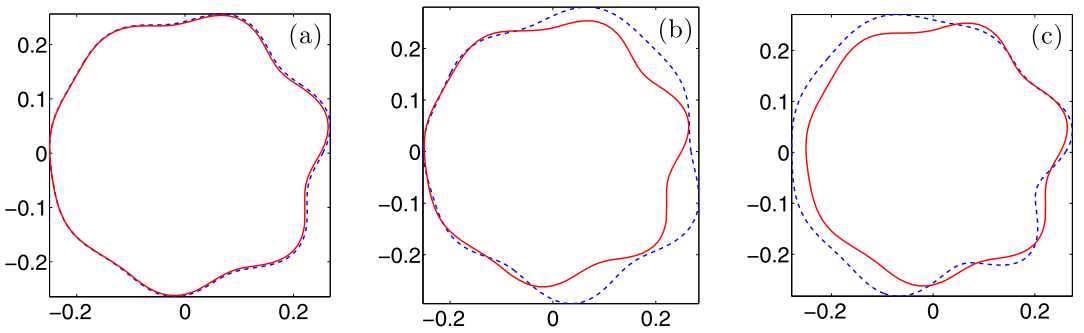

Fig. 8. Limited aperture data: Exact (solid line) and reconstructed (dashed line) surface function for $\varepsilon = 0.02$, $\delta = 1\%$, $h = 0.03\lambda$ and incident plane wave from left, using (a) full aperture data; (b) data on the left half circle; (c) data on the right half-circle.

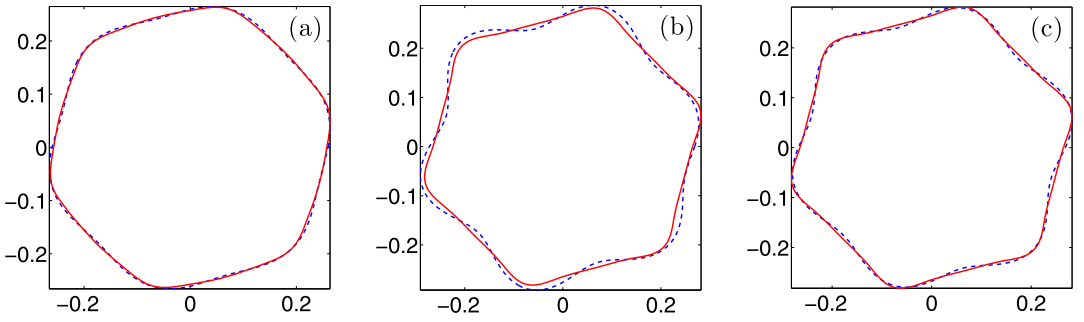

Fig. 9. Example 2: Exact (solid line) and reconstructed (dashed line) surface function for $\delta = 0$, $h = 0.1\lambda$. (a) $\varepsilon = 0.02$; (b) $\varepsilon = 0.04$; (c) $\varepsilon = 0.04$ and after 5 iterations of nonlinear correction.

may be measured only in certain range of angles in many practical situations. Compared to full aperture problem, limited aperture problems are more challenging since the ill-posedness and nonlinearity of the problems become more severe.

Now we test our method with limited aperture data. Let $a = \lambda/4$, $\varepsilon = 0.02$, $\delta = 1\%$, $h = 0.03\lambda$ be fixed and the incident field be a plane wave from the left. Fig. 8 shows the results using full aperture data, the data on the left half circle and the data on the right half circle respectively. The missing data are treated as zero in the limited aperture cases. It can be observed that we are still able to achieve relatively good reconstruction on the side of the obstacle where the measurements are taken. The reconstruction on the side of the obstacle in the "shadow" region is deteriorated due to the loss of information.

5.2. Example 2

Consider an obstacle with surface given by $r(\theta) = a + f(\theta)$, where $a = \lambda/4$, $f = \varepsilon g$ and

$$g(\theta) = \lambda e^{\sin 6\theta - 1}.$$

This example is more difficult than the previous one since the surface function contains infinitely many Fourier modes. Nevertheless we observe similar effects of the parameters on the reconstructions. Thus we shall not present all the investigation results but only the effect of ε and the nonlinear correction. The truncation level in (3.20) and (4.4) is taken as $N = K = 6$. The incident field is a single plane wave propagating in the direction $\theta = 0$. Let $\delta = 0$, $h = 0.1\lambda$ be fixed. Fig. 9(a) and Fig. 9(b) show the exact (solid) and the reconstructed (dashed) profile for $\varepsilon = 0.02$ and $\varepsilon = 0.04$ respectively. Fig. 9(c) shows the result for $\varepsilon = 0.04$ and after 5 iterations of nonlinear correction. As expected, the overall accuracy is relatively lower than that in example 1 for similar values of the parameters.

6. Conclusion

We considered an inverse obstacle scattering problem in the near-field by using any time-harmonic wave. The obstacle was assumed to be a small and smooth perturbation of a disk. The measurement data was taken at a circle surrounding the obstacle. We reformulated the scattering problem as a boundary value problem with Dirichlet and transparent boundary conditions on the boundary of the obstacle and the artificial boundary on the measurement circle respectively. Using the transformed field expansion, we reduced the two-dimensional boundary value problem into a successive sequence of one-dimensional two-point boundary value problems, which were solved in closed forms. By truncating the infinite linear system and dropping higher order terms in the power series expansion, we obtained an approximate but explicit and linear

relation between the Fourier coefficients of the solution and the data, which was used to reconstruct the shape of the obstacle. In addition, we presented a simple nonlinear correction algorithm to improve the accuracy of the reconstruction for large deformation parameters. Numerical examples show that the method is efficient and stable to reconstruct the shape of obstacles with subwavelength resolution.

The presented method can be readily extended to other boundary conditions and transmission problems. The extension to the three-dimensional geometry is also relatively straightforward by using the spherical harmonics expansion. A challenging problem is to consider obstacles with general shapes and larger deformations. Other interesting future works include the convergence analysis of the proposed method, near-field imaging of multiple obstacles, and multi-scale or random surfaces.

References

[1] G. Bao, T. Cui, P. Li, Inverse diffraction grating of Maxwell's equations in biperiodic structures, Opt. Express 22 (2014) 4799–4816.
[2] G. Bao, P. Li, Near-field imaging of infinite rough surfaces, SIAM J. Appl. Math. 73 (2013) 2162–2187.
[3] G. Bao, P. Li, Near-field imaging of infinite rough surfaces in dielectric media, SIAM J. Imaging Sci. 7 (2014) 867–899.
[4] G. Bao, P. Li, Convergence analysis in near-field imaging, Inverse Probl. 30 (2014) 085008.
[5] G. Bao, J. Lin, Imaging of local surface displacement on an infinite ground plane: the multiple frequency case, SIAM J. Appl. Math. 71 (2011) 1733–1752.
[6] G. Bao, J. Lin, Imaging of reflective surfaces by near-field optics, Opt. Lett. 37 (2012) 5027–5029.
[7] G. Bao, J. Lin, Near-field imaging of the surface displacement on an infinite ground plane, Inverse Probl. Imaging 2 (2013) 377–396.
[8] F. Cakoni, D. Colton, Qualitative Methods in Inverse Scattering Theory: An Introduction, Springer, Berlin, 2005.
[9] P. Carney, J. Schotland, Near-field tomography, in: G. Uhlmann (Ed.), Inside Out: Inverse Problems and Applications, Cambridge University Press, 2003, pp. 133–168.
[10] T. Cheng, P. Li, Y. Wang, Near-field imaging of perfectly conducting grating surfaces, J. Opt. Soc. Am. A 30 (2013) 2473–2481.
[11] D. Colton, A. Kirsch, A simple method for solving inverse scattering problems in the resonance region, Inverse Probl. 12 (1996) 383–393.
[12] D. Colton, R. Kress, Inverse Acoustic and Electromagnetic Scattering Theory, Springer-Verlag, Berlin, 2012.
[13] D. Courjon, Near-Field Microscopy and Near-Field Optics, Imperial College Press, London, 2003.
[14] NIST Digital Library of Mathematical Functions, http://dlmf.nist.gov/, Release 1.0.6 of 2013-05-06.
[15] F. Hettlich, Frechét derivatives in inverse obstacle scattering, Inverse Probl. 11 (1995) 371–382.
[16] G. Hu, J. Yang, B. Zhang, H. Zhang, Near-field imaging of scattering obstacles with the factorization method, Inverse Probl. 30 (2014) 095005.
[17] M. Ikehata, Reconstruction of an obstacle from the scattering amplitude at a fixed frequency, Inverse Probl. 14 (1998) 949–954.
[18] A. Kirsch, The domain derivative and two applications in inverse scattering theory, Inverse Probl. 9 (1993) 81–96.
[19] A. Kirsch, The music algorithm and the factorization method in inverse scattering theory for inhomogeneous media, Inverse Probl. 18 (2002) 1025–1040.
[20] R. Kress, Newton's method for inverse obstacle scattering meets the method of least squares, Inverse Probl. 19 (2003) 91–104.
[21] R. Kress, W. Rundell, A quasi-Newton method in inverse obstacle scattering, Inverse Probl. 10 (1994) 1145–1157.
[22] P. Li, Y. Wang, Near-field imaging of obstacles, Inverse Probl. Imaging 9 (2015) 189–210.
[23] P. Li, Y. Wang, Near-field imaging of interior cavities, Commun. Comput. Phys. 17 (2015) 542–563.
[24] R. Potthast, Stability estimates and reconstructions in inverse acoustic scattering using singular sources, J. Comput. Appl. Math. 114 (2000) 247–274.
[25] R. Schmidt, Multiple emitter location and signal parameter estimation, IEEE Trans. Antennas Propag. 34 (1986) 276–280.